Soil–Geogrid Interaction at Various Influencing Factors by Pullout Tests with Applications of FBG Sensors

Han-Lin Wang, Ph.D., A.M.ASCE[1]; Ren-Peng Chen, M.ASCE[2]; Qi-Wei Liu[3]; Xin Kang, A.M.ASCE[4]; and Yan-Wei Wang[5]

Abstract: The behavior of soil–geogrid interaction is a dominant factor in the long-term performance of geogrid-reinforced earth structures. This study investigates the interaction of sandy soil and the embedded geogrid by pullout tests with the application of a novel testing method using fiber Bragg grating (FBG) sensors. Three influencing parameters are considered: dry density of soil, initial normal stress, and fixing condition of the pullout back end. A displacement-controlled mode is used for the normal stress, and the pullout load is applied at a constant loading rate. The results indicate that for the case with a free back end, the peak shear stress mobilizes from the front face toward the back end with the elongation of the geogrid during the pullout process, before the entire slippage of the geogrid. With higher dry density or higher initial normal stress, the mobilization of the peak shear stress transmits more slowly and the distribution area of shear stress along the geogrid is accordingly narrower due to the corresponding higher resistance by the soil particles. However, the values of the peak shear stress in these two cases are still higher than in cases with lower dry density or lower initial normal stress. By contrast, a different distribution mode of shear stress along the soil–geogrid interface is identified for geogrid with a fixed back end, with maximum shear stress developing near the front face for all pullout displacements. **DOI: 10.1061/(ASCE)MT.1943-5533.0002537.**

Author keywords: Soil–geogrid interaction; Fiber Bragg grating (FBG); Pullout test; Dry density; Fixing condition.

Introduction

As an effective reinforcing inclusion layer embedded in soil, geogrid has been extensively used to deal with geotechnical problems in practice, such as in the field of slopes, embankments, retaining walls, and some other earth structures (Leshchinsky et al. 2010; Al-Qadi et al. 2012; Han et al. 2012; Chen et al. 2013, 2014b, 2016; Qian et al. 2013; Abdesssemed et al. 2015; Zhao et al. 2016; Sun et al. 2017a; Wang et al. 2018a, b). During the service life of these structures, the soil–geogrid interaction plays a key role in the reinforcing behaviors. Therefore, assessing the soil–geogrid interaction is of paramount importance to maintain the long-term performance of the reinforced structures.

The behavior of soil–geogrid interaction is complex, with various influencing factors, such as normal stress (overburden pressure), soil properties, stiffness of the front face, geogrid stiffness, number of transverse and longitudinal members, loading rate, and so on (Lopes and Ladeira 1996; Sugimoto et al. 2001; Sugimoto and Alagiyawanna 2003; Moraci and Recalcati 2006; Teixeira et al. 2007; Zhang et al. 2007; Liu et al. 2009; Palmeira 2009; Zhang and Yasufuku 2009; Abu-Farsakh et al. 2012; Arulrajah et al. 2014). In general, the failure of geogrid can be categorized into two cases under pullout conditions: pullout failure, with significant overall slippage in the soil; and tensile failure, probably with anchorage at the back end. To date, the soil–geogrid interaction related to the pullout failure has been widely studied, whereas fewer investigations of the tensile failure with fixed back end have been reported (Palmeira 2009; Wang et al. 2014). Moreover, the comparison of these two cases is still scarce. With regard to the effect of the dry density of soil, the pullout behavior of geogrid was studied by Lopes and Ladeira (1996), Zhang et al. (2007), and Zhang and Yasufuku (2009). Nevertheless, the behavior of soil–geogrid interaction has not been fully addressed, and this issue still needs to be clarified.

In terms of the evaluation methods of soil–geogrid interaction, both the finite-element method (FEM) and the discrete-element method (DEM) are widely applied (Sugimoto and Alagiyawanna 2003; McDowell et al. 2006; Ferellec and McDowell 2012; Chen et al. 2014a; Wang et al. 2014). On the other hand, experimental approaches, such as pullout tests, are also commonly considered to investigate this behavior. To estimate the deformation of geogrid during the pullout tests, nonextensible steel wire is generally used to connect a specific location of the geogrid with the other end, integrated with a corresponding LVDT sensor or dial gauge outside the pullout box (Wilson-Fahmy et al. 1994, 1995; Sugimoto et al. 2001; Sugimoto and Alagiyawanna 2003; Moraci and Recalcati 2006; Teixeira et al. 2007; Ferreira and Zornberg 2015). Although this method provides reasonable testing results according to these studies, the estimations using this method are indirect and complicated, and require calculating several equations. In addition,

[1]Research Fellow, Ministry of Education Key Laboratory of Building Safety and Energy Efficiency, College of Civil Engineering, Hunan Univ., Changsha 410082, China; Postdoctoral Fellow, Dept. of Civil and Environmental Engineering, Faculty of Science and Technology, Univ. of Macau, Macau, China. Email: wanghanlin@zju.edu.cn

[2]Professor, Ministry of Education Key Laboratory of Building Safety and Energy Efficiency, College of Civil Engineering, Hunan Univ., Changsha 410082, China (corresponding author). Email: chenrp@hnu.edu.cn

[3]Ph.D. Candidate, Ministry of Education Key Laboratory of Building Safety and Energy Efficiency, College of Civil Engineering, Hunan Univ., Changsha 410082, China.

[4]Professor, Ministry of Education Key Laboratory of Building Safety and Energy Efficiency, College of Civil Engineering, Hunan Univ., Changsha 410082, China.

[5]Engineer, Ningbo Jiangong Jianle Engineering Co. Ltd., Ningbo 315040, China.

Note. This manuscript was submitted on March 6, 2018; approved on June 14, 2018; published online on October 24, 2018. Discussion period open until March 24, 2019; separate discussions must be submitted for individual papers. This paper is part of the ***Journal of Materials in Civil Engineering***, © ASCE, ISSN 0899-1561.

the testing setup is also complex and costly, with several LVDT sensors in addition to the pullout box.

A newly developed testing technology based on the theory of light propagation, strain-sensitive fiber Bragg gratings (FBG) have been used as sensing elements in optical fiber sensors in recent decades. As the light travels, the reflected wavelength—namely the Bragg wavelength (in a narrow band)—of the FBG sensor is used to estimate the strain in a structure. Under external loading or temperature variation, deformation or strain may develop in structures. Accordingly, the Bragg wavelength of the integrated FBG sensors changes in the reflected wavelength spectrum, which can be recorded by the optical interrogator. Using the precalibrated relationship between the strain of the specific structure and the wavelength shift of the FBG sensor, the corresponding strain can be estimated. Compared with conventional electrical sensors, FBG sensors have advantages of high sensitivity, high resolution, fast response, and immunity to electrical and electromagnetic signals (Nichols et al. 2007; Mihailov 2012; Mamidi et al. 2014; Hussaini et al. 2015; Chen et al. 2016). To date, the testing method with FBG sensors has been used in several geotechnical areas (Lee et al. 2004; Ho et al. 2006; Hussaini et al. 2015; Wang et al. 2015; Chen et al. 2016; Hong et al. 2016; Sun et al. 2017b). However, the reliability of the application of FBG sensors to evaluate the soil–geogrid interaction in pullout tests remains unknown.

This study conducted pullout tests on geogrid embedded in sandy soil, with various dry densities of soil, initial normal stresses, and fixing conditions at the back end. The normal stress was applied in a displacement-controlled mode and the pullout process was performed under a constant loading speed. FBG sensors were first calibrated and then were integrated at different locations of the geogrid to investigate the strain behavior. During the tests, pullout force, pullout displacement, normal stress, and wavelength shift of the FBG sensors were monitored. The effects of the three aforementioned influencing factors on the soil–geogrid interaction behavior are analyzed and discussed.

Testing Setup and Materials

Pullout Testing Apparatus

The schematic view and a photograph of the pullout testing apparatus are shown in Figs. 1 and 2, respectively. The apparatus mainly

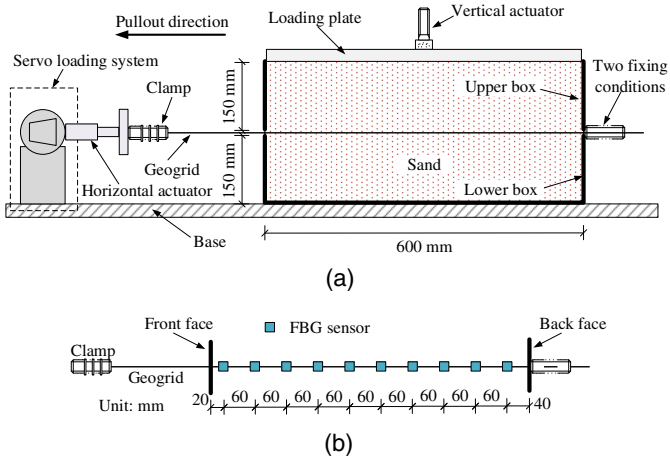

Fig. 1. Schematic view of pullout testing apparatus: (a) cross section; and (b) FBG sensors on the geogrid (four tests).

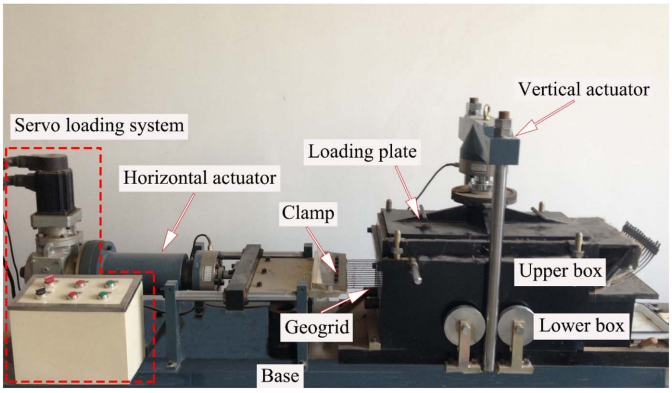

Fig. 2. Pullout testing apparatus. (Image by Yan-Wei Wang.)

consisted of two pullout boxes, two clamps, a loading plate, a vertical actuator, a horizontal actuator, and a servo loading system.

The upper box and lower box were made of 10-mm-thick steel, with inner dimensions of 600 × 300 × 150 mm (length × width × height) for each box. During the pullout test, the two boxes were fixed to each other, leaving two openings 300 mm wide and 10 mm high at the front and back faces for the installation of the geogrid. Two plane clamps were provided. The clamp at the front face was fixed to the geogrid in all tests, whereas the fixing condition between the geogrid and the clamp at the back face defined the two tests: a free-end test with no fixing, and a fixed-end test with fixing. The front clamp was connected to a horizontal actuator to apply the pullout load. After the sample preparation in the pullout box, a loading plate was lowered to contact the leveled surface of the sample to ensure the homogeneity of the normal stress applied by the vertical actuator. For this apparatus, both the horizontal and vertical actuators were controlled by the servo loading system. Both actuators were integrated with a force sensor (range 50 kN; accuracy ±0.1% full scale) and LVDT (linear variable differential transducer; range 300 mm; accuracy ±0.04 mm) to monitor the force and displacement, respectively, in pullout and normal stress directions.

Geogrid and Fiber Bragg Grating Sensor

This study used a commonly used uniaxial geogrid made of polypropylene (PP). Table 1 lists the properties of this material. For a single span of the geogrid, the length of the longitudinal rib was 500 mm and the interval between two adjacent longitudinal ribs was 20 mm. Because of the width of the pullout box (300 mm),

Table 1. Properties of geogrid

Geogrid part	Parameter	Value
Whole geogrid	Ultimate longitudinal tensile strength, T_u	130.6 kN/m
	Longitudinal strain at T_u	8.22%
	Geogrid solid area/total area	22.6%
	Stiffness at strain of 2%	2,459.5 kN/m
Longitudinal rib	Length	500 mm
	Width	4.2 mm
	Thickness	1.6 mm
	Interval between two adjacent longitudinal ribs	20 mm
	Number of longitudinal ribs (in this study)	15
Transverse rib	Length (in this study)	280 mm
	Width	20 mm
	Thickness	5.6 mm

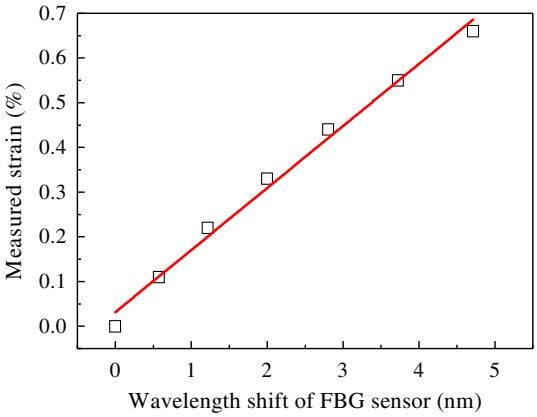

Fig. 3. Calibration of FBG sensor.

geogrids with an overall width of 280 mm were chosen for the tests. In other words, the examined geogrids contained 15 longitudinal ribs. Considering the length of the pullout box (600 mm), geogrids with two spans (three transverse ribs with total length equaling 1,000 mm) were selected. During the sample preparation, the middle transverse rib was located in the middle of the pullout box (300 mm from the front face) in all tests.

In four tests, fiber Bragg grating sensors were integrated in the middle longitudinal rib of the geogrid. The distribution of the FBG sensors is shown in Fig. 1(b). For one FBG sensor, an optical fiber was used, composed of a core, a cladding, and a coating. The core was a cylindrical rod of dielectric material with 8–10 μm diameter, allowing long-range transmission of light. The cladding was used to wrap the core to ensure proper light propagation through the core without the interference of the surrounding environment. To protect the fiber from being damaged by environmental agents, the cladding was covered with a coating made of acrylate. The Bragg grating was photoetched inside the core of an optical fiber along a short section (<10 mm) by exposure to an ultraviolet interference pattern. This grating structure is also known as the periodic demodulation of the refractive index of optical fiber core. During testing, the FBG sensors were connected to a data acquisition system (MOI sm130, produced by Micron Optics, Atlanta, Georgia). Using this grating structure, the Bragg wavelength can be determined by the reflection signal of light with a narrow band. In this study, the testing Bragg wavelength of this sensor ranged from 1,510 to 1,590 nm and the testing error remained within $\pm$0.2 nm. Under structure deformation or temperature change, the Bragg wavelength shifts due to the expansion or contraction of the Bragg grating. In this way, the strain information can be obtained using the wavelength shift.

To integrate the FBG sensor into the geogrid rib, the surface of the rib was first ground with sandpaper and washed with water cotton to ensure full contact between the FBG sensor and the geogrid rib. Then the FBG sensor was fixed on the geogrid rib with epoxy and waterproof tape. Before the pullout tests, the FBG sensor attached to this geogrid was calibrated using a universal testing machine at a constant temperature condition. The strain of the geogrid and the wavelength shift of the FBG sensor were measured by an electrical strain gauge and the FBG sensor mounted on the surface of the longitudinal rib, respectively (Chen et al. 2016). The testing results are presented in Fig. 3. A proper linear relationship was presented between the measured strain of the geogrid and the wavelength shift data measured by the FBG sensor. Hence, the calibration result in Fig. 3 was also used to calculate the axial strain of the geogrid ε in the pullout tests. Then the tensile force per unit width of the geogrid T_r was determined using the following equation:

$$T_r = \frac{F}{W} = \frac{J\varepsilon W}{W} = J\varepsilon \tag{1}$$

where F = tensile force across the width of the geogrid; J = stiffness parameter [2,459.5 kN/m (Table 1)], which is defined as the force needed to cause a unit axial strain (longitudinal) in the geogrid for a unit width (ASTM 2015); and W = width of the testing geogrid in the pullout tests (0.28 m in this study).

With the tensile forces measured by the adjacent FBG sensors, the mean shear stress τ_i along the ith segment was estimated as

$$\tau_i = \frac{T_{ri-1} - T_{ri}}{\Delta s} \tag{2}$$

where T_{ri-1} and T_{ri} = tensile forces measured at the front and back end of the ith segment, respectively; and Δs = distance between the FBG sensors.

Testing Soil

Sand from a filling site in Hangzhou, China was used in all tests. This sand is commonly applied as the protective cushion for the geogrid layer in the geosynthetic-reinforced pile-supported embankment of this region (Chen et al. 2016; Wang et al. 2018a, b). The grain-size distribution curve is shown in Fig. 4. The coefficient of uniformity C_u and coefficient of curvature C_c were determined as 2.83 and 0.77, respectively. According to ASTM (2017), the testing sand is classified as poorly graded sand (SP), which is also widely used as standard model soils for investigating soil–interface problems in the literature (Kang et al. 2012).

Testing Procedures

This study investigated the effects of dry density of soil ρ_d, initial normal stress σ_{n0}, and fixing condition of the back end. Table 2 lists the experimental details. During the sample preparation, the water content of the sand was controlled at 4.0% (natural water content) for all tests. The sand was oven-dried, and water was added and mixed with the dry sand to obtain the target water content. After mixing, the wet sand was stored in a hermetic container for 24 h for moisture homogenization. Then the mass of the wet sand was calculated based on the target dry density, water content, and the volume of the pullout testing apparatus.

Before putting sand into the pullout box, the inner walls of the pullout box were lubricated with grease to reduce friction along these boundaries. The soil samples were prepared using the following compaction method, which was also used in several studies to assure the relatively uniform sample with predetermined

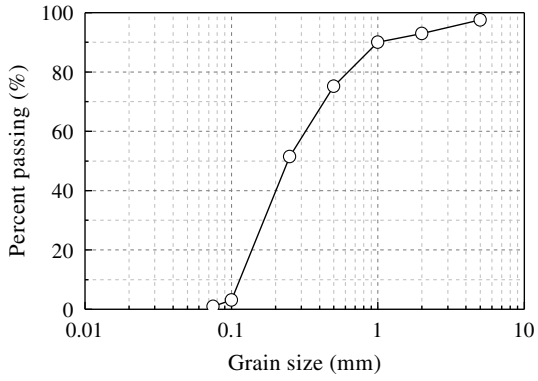

Fig. 4. Grain-size distribution of sand.

Table 2. Experimental details

Variables	Test number	ρ_d (g/cm^3)	σ_{n0} (kPa)	Back-end fixing	With FBG sensor
Dry density of soil	1	1.51	80	Free	No
	2	1.57	80	Free	Yes
	3	1.68	80	Free	Yes
Initial normal stress	4	1.68	3	Free	No
	5	1.68	20	Free	No
	6	1.68	50	Free	Yes
	3	1.68	80	Free	Yes
	7	1.68	200	Free	No
Fixing condition of back end	6	1.68	50	Free	Yes
	8	1.68	50	Fixed	No
	3	1.68	80	Free	Yes
	9	1.68	80	Fixed	Yes

Note: ρ_d and σ_{n0} represent dry density of soil and initial normal stress, respectively.

dry density (Indraratna et al. 1993; Trinh et al. 2012; Wang et al. 2017, 2018c, d). First, sand with a specific mass was placed into the lower box homogeneously in three layers with a thickness of 50 mm for each layer. A metal tamp (rectangular bottom 220 × 220 mm and a total weight of 16 kg, with compaction energy provided by a vibration pump) was used to compact the sample to achieve the desired thickness corresponding to the expected dry density. After the sand sample was placed in the lower box, a geogrid 1,000 mm long and 280 mm wide was set on the top of the leveled surface. The front end was connected to the plane clamp by tightening seven bolts (Figs. 1 and 2); the fixing condition of the back end depended on the testing condition (Table 2). To ensure the tightness between the clamp and front end of the geogrid, two pieces of geotextiles were set between them. In this way, an even force was applied across the geogrid width through the clamp. In four tests, FBG sensors were integrated with the geogrid [Fig. 1(b) and Table 2]. Then the upper box was installed and fixed to the lower box. Like the sample preparation in the lower box, sand with a predetermined mass was also placed in three layers and tamped to the target dry density in the upper box.

For the loading process, the loading plate was lowered to be in contact with the leveled surface of the sand sample and the normal stress was applied through the vertical actuator. This study used the displacement-controlled loading mode for the normal stress to directly investigate the dilative behaviors of soil, with the loading plate controlled at a constant location during the loading process. Due to the dilatancy of soil, biased improvement of soil might develop during the pullout process. Because the same loading method was applied for the normal stress, the improvement effect was not considered in the following analysis. After the application of normal stress, the geogrid was pulled out by the horizontal actuator at a constant rate of 1 mm/min, which is commonly used in the pullout tests (Huang and Bathurst 2009). The tests terminated when the maximum pullout displacement (100 mm) or the peak pullout force was reached.

Results and Discussions

Effect of Dry Density

This section demonstrates the testing results including the variations of pullout force, normal stress, tensile force, and shear stress along soil–geogrid interface for different dry densities in Tests 1, 2, and 3 (Table 2). The pullout force and tensile force discussed in this study both indicate the force per unit width of the geogrid.

Pullout Force and Normal Stress

Fig. 5 shows the variation of pullout force with the pullout displacement for different dry densities. On the whole, the pullout force increased rapidly in the beginning and tended to become stable as the pullout displacement continued to increase. For a given pullout displacement, the pullout force at higher dry density was higher, which agrees with the discrete-element method investigations conducted by Zhang et al. (2007) and the experimental studies carried out by Zhang and Yasufuku (2009).

The variation of normal stress with pullout displacement is plotted in Fig. 6. Because a displacement-controlled loading mode was applied for the normal stress, this value may change during the

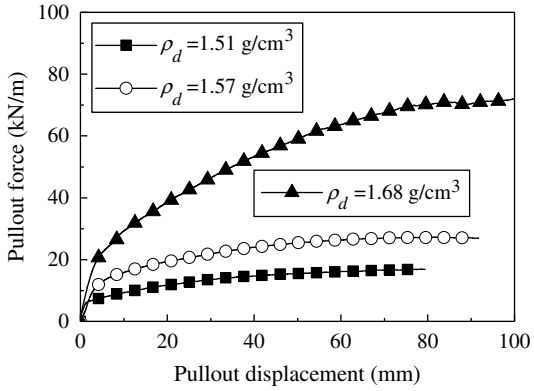

Fig. 5. Comparison of dry densities: variations of pullout force with pullout displacement.

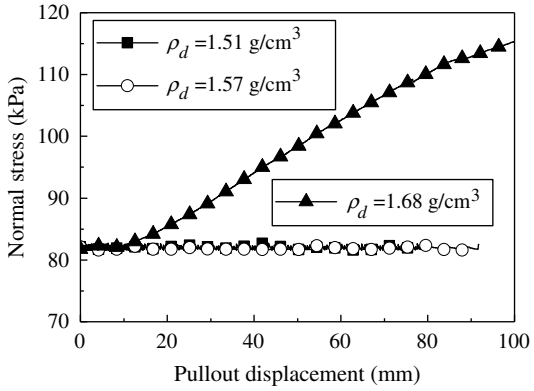

Fig. 6. Comparison of dry densities: variations of normal stress with pullout displacement.

pullout process, induced by the movement of the soil particles. In the pullout test, both elongation and slippage of the geogrid occur at the same time (Sugimoto and Alagiyawanna 2003). For lower dry densities ($\rho_d = 1.51$ and 1.57 g/cm^3), the normal stresses stayed relatively stable at the initial value, suggesting that slight soil dilatancy developed during the tests and the overall slippage of geogrid was dominant without causing significant movement of the loose sand particles. By contrast, at $\rho_d = 1.68$ g/cm^3, the normal stress increased by about 30 kPa at 100 mm pullout displacement compared with the initial status. For this case, significant dilatancy of the soil was produced and more noticeable elongation of the geogrid developed.

Tensile Force and Shear Stress

To better understand the effect of soil dry density on the soil–geogrid interaction behavior, the measured results from the FBG sensors in Tests 3 and 2 (Table 2) are compared in Fig. 7, which plots variations of tensile force of the geogrid with the pullout displacement at different locations [Figs. 7(a and b)], and distributions of tensile force [Figs. 7(c and d)] and shear stress [Figs. 7(e and f)] along the geogrid length at various pullout displacements. To investigate the stress mobilization at the soil–geogrid interface, the data for small pullout displacement of less than 5 mm (before entire slippage of the geogrid) are compared. In Fig. 7, S_i and s represent the distance of the sensor location from the front face of the pullout

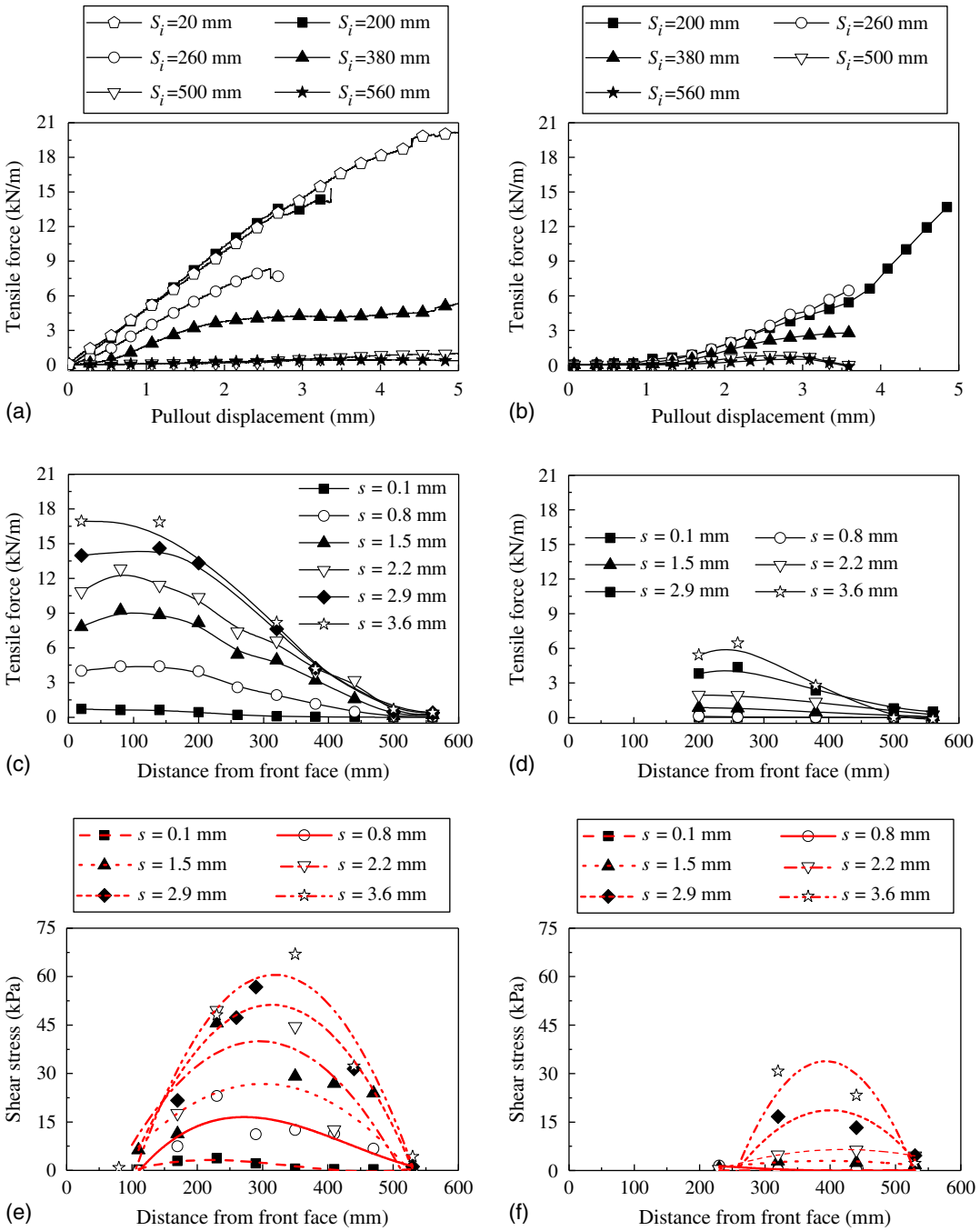

Fig. 7. Comparison of dry densities: (a and b) variations of tensile force with pullout displacement; (c and d) variations of tensile force with distance from front face; and (e and f) variations of shear stress with distance from front face. (a, c, and e) indicate the Test 3 with 1.68 g/cm^3 dry density; and (b, d, and f) indicate the Test 2 with 1.57 g/cm^3 dry density.

box and the pullout displacement, respectively. Because of a technical problem, data from the sensors located at $S_i = 20$–140 mm were not recorded for the case of 1.57 g/cm^3 dry density; the existing measured data (Fig. 7) for this case could still interpret the soil–geogrid interaction well.

The tensile force of the geogrid part close to the front face increased rapidly as the pullout displacement increased [Figs. 7(a and b)]. As S_i increased, the increasing rate of the tensile force decreased. In particular, the tensile forces changed slightly when $S_i \geq 500$ mm (close to the back end) for both cases in this range of pullout displacement. The tensile force distributions along the geogrid length are more clearly shown in Figs. 7(c and d). At a given pullout displacement, the maximum tensile force developed in the vicinity of the front face. The value of the tensile force decreased nonlinearly to the back end, showing negligible values of tensile force when $S_i \geq 500$ mm. The aforementioned phenomena indicate that the elongation of the geogrid first developed at the location near the front face after the prompt application of the pullout displacement. As the pullout displacement increased, the strain of the elongated part continued to increase until tensile failure, and the elongation behavior also tended to transmit toward the back end.

On the other hand, the effect of the soil dry density on the tensile force of the geogrid was distinct [Figs. 7(c and d)]. At a given pullout displacement at locations $S_i < 500$ mm, where the geogrid started to elongate, the tensile force was higher for the sample with higher dry density. This suggests that the deformation of geogrid embedded in the denser sample was more significant, whereas more localized slippage behavior of the geogrid was identified for the looser sample.

To investigate the soil–geogrid interaction behavior, the shear stress along the geogrid length was calculated using Eq. (2) [Figs. 7(e and f)]. Quadratic polynomial fitting methods ($y = ax^2 + bx + c$) were used to fit the measured data. Table 3 lists the coefficients of determination R^2, i.e., the square of the Pearson correlation coefficient between the testing results and the fitting outcomes (Devore 2011) for the fitting curves. When the pullout displacement exceeded 2.2 mm, the fitting curves well predicted the testing results, with R^2 values higher than 0.900. For the case of $\rho_d = 1.68$ g/cm^3, a peak shear stress was identified for all cases [Fig. 7(e)]. This peak point mobilized from the front face toward the back end as the pullout displacement increased, which indicates that the elongation was also transmitted to the back end. After this peak point reached the back end and the entire elongation of the geogrid was less than the pullout displacement, the overall slippage occurred. This observation about the mobilization of the shear stress is consistent with the illustrations by Sugimoto et al. (2001) and Sugimoto and Alagiyawanna (2003). Furthermore, the peak shear strength clearly showed in the middle part of the geogrid when $s \geq 0.8$ mm for $\rho_d = 1.68$ g/cm^3, with the part near the front face presenting smaller values [Fig. 7(e)]. This might be because in the vicinity of the front face, as the pullout displacement increases, more soil particles move with the elongation of this part, and thus the relative soil–geogrid displacement is smaller, leading to a lower shear stress. To better clarify the issue about the micromechanism of relative soil–geogrid displacement, more studies are needed. Compared with the case of higher dry density, the shear stress at the soil–geogrid interface had lower values for the looser samples at a given pullout displacement [Fig. 7(f)]. Furthermore, due to less resistance of the soil particles, the location of the peak shear stress for the looser sample was closer to the back end than in the case with denser soil. This in turn led to less movement or rearrangement of the sand particles during the pullout process for the looser sample. As a result, less or even negligible soil dilatancy occurred in these samples, corresponding well with the observations in Fig. 6.

Table 3. Coefficients of determination for fitting curves

s (mm)	Test 2	Test 3	Test 6	Test 9
0.1	0.402	0.885	0.720	0.393
0.8	0.924	0.745	0.553	0.736
1.5	0.868	0.431	0.610	0.573
2.2	0.999	0.687	0.717	0.652
2.9	0.913	0.952	0.900	0.848
3.6	0.930	0.930	—	—

Note: s = pullout displacement.

Effect of Initial Normal Stress

As in the previous section, the effect of initial normal stress on the variations of pullout force, normal stress, tensile force and shear stress at the soil–geogrid interface were interpreted in Tests 4, 5, 6, 3, and 7 (Table 2).

Pullout Force and Normal Stress

Fig. 8 plots the variations of pullout force against the pullout displacement for different initial normal stresses. In all cases, the variation trend of the pullout force was similar to that illustrated previously: a rapid increase of pullout force with the pullout

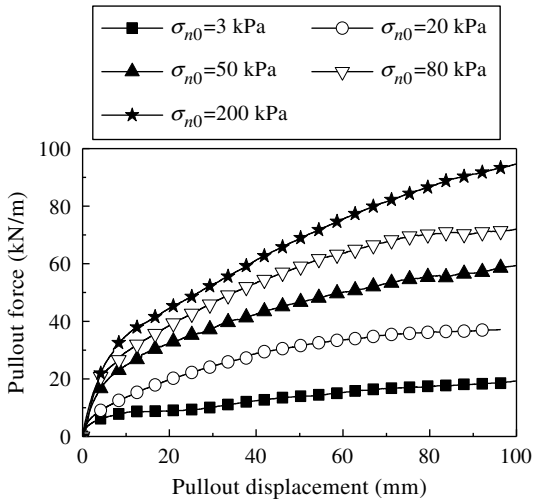

Fig. 8. Comparison of initial normal stresses: variations of pullout force with pullout displacement.

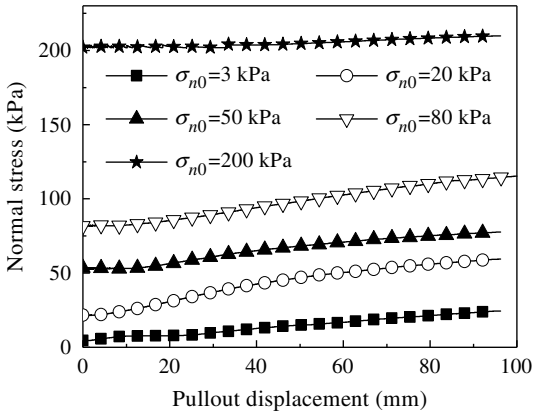

Fig. 9. Comparison of initial normal stresses: variations of normal stress with pullout displacement.

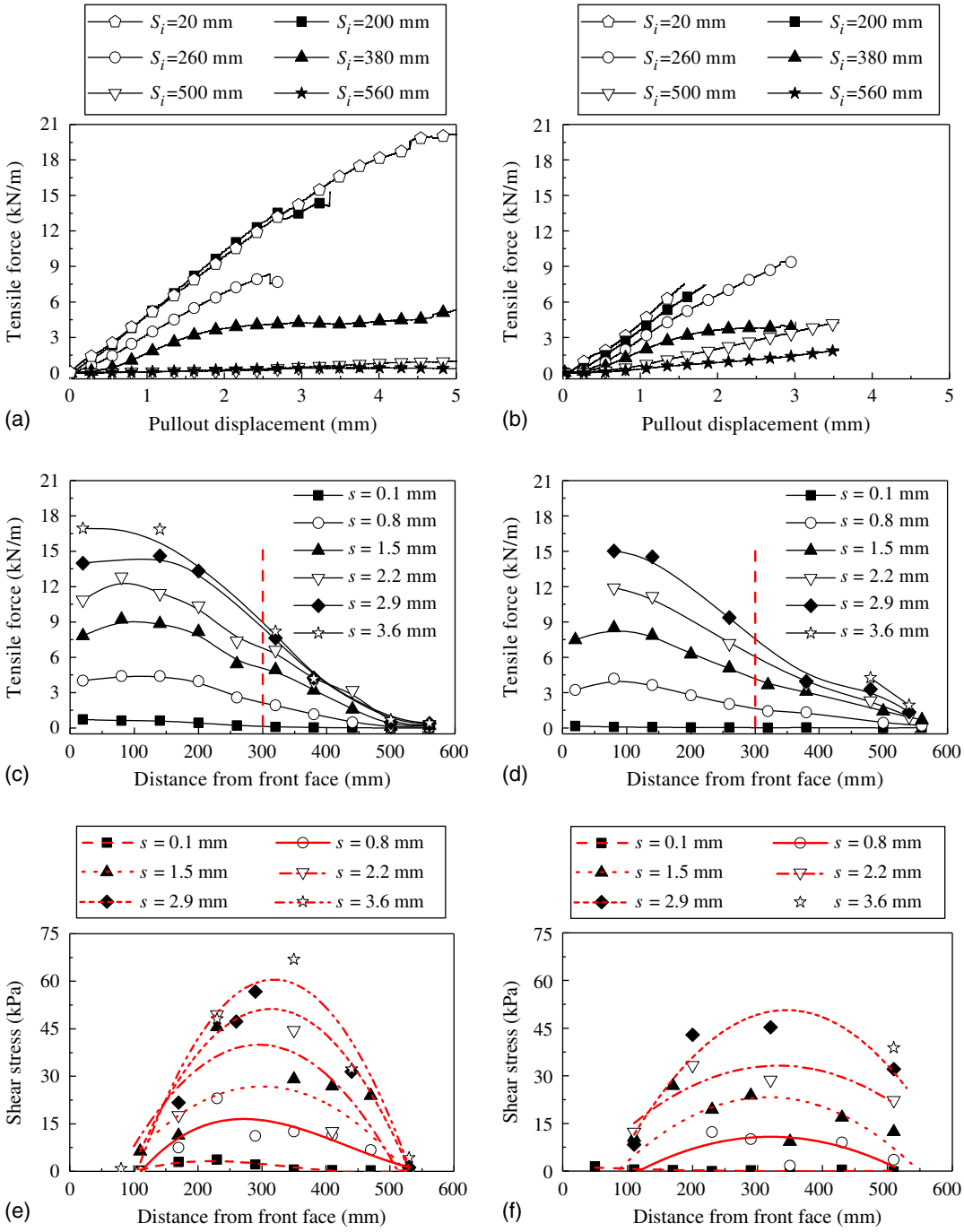

Fig. 10. Comparison of initial normal stresses: (a and b) variations of tensile force with pullout displacement; (c and d) variations of tensile force with distance from front face; and (e and f) variations of shear stress with distance from front face. (a, c, and e) indicate the Test 3 with 80 kPa initial normal stress; and (b, d, and f) indicate the Test 6 with 50 kPa initial normal stress.

displacement increasing in the beginning, followed by a less significant variation. As the initial normal stress increased, the pullout force increased at a given pullout displacement, suggesting higher soil resistance under a higher initial normal stress.

Fig. 9 presents the effect of initial normal stress on the variations of normal stress versus the pullout displacement. At a pullout displacement of 90 mm, the normal stress increased by 4.11%, 1.69%, 0.44%, 0.37%, and 0.04% compared with the initial state for the cases of $\sigma_{n0} = 3$, 20, 50, 80, and 200 kPa, respectively. It can be concluded that under higher initial normal stress, the increment ratio of the normal stress is lower during the pullout process.

Tensile Force and Shear Stress

In order to investigate the effect of initial normal stress on the soil–geogrid interaction behaviors, Fig. 10 shows the measured results of the FBG sensors in Tests 3 and 6 (Table 2) at $\sigma_{n0} = 80$ and 50 kPa.

The variation curves of tensile force for $\sigma_{n0} = 50$ kPa were distributed in a narrower range than those for $\sigma_{n0} = 80$ kPa [Figs. 10(a and b)]. The difference of tensile force between two locations was thus less significant for $\sigma_{n0} = 50$ kPa, except at $S_i > 500$ mm, where negligible elongation was identified for $\sigma_{n0} = 80$ kPa. For the geogrid part closer to the front face ($S_i \leq 300$ mm), the tensile

force was slightly higher for $\sigma_{n0} = 80$ kPa than for $\sigma_{n0} = 50$ kPa at a given pullout displacement [Figs. 10(c and d)]. However, when $S_i > 300$ mm, which was closer to the back end, the values of tensile force for $\sigma_{n0} = 50$ kPa were larger than for the $\sigma_{n0} = 80$ kPa case [Figs. 10(c and d)]. This was because for the small pullout displacement (less than 5 mm), the elongation of geogrid had not reached $S_i > 500$ mm for $\sigma_{n0} = 80$ kPa, whereas this part of geogrid for $\sigma_{n0} = 50$ kPa started to elongate, leading to higher values of tensile force in the vicinity. In other words, the elongation of the geogrid spread more widely for $\sigma_{n0} = 50$ kPa because of less resistance by the soil particles. Nevertheless, at $S_i \leq 300$ mm, the tensile force still had higher values under higher initial normal stress, with more-pronounced elongated behavior.

In terms of the shear stress, quadratic polynomial fitting methods were also applied to fit these data [Figs. 10(e and f)], with the coefficients of determination listed in Table 3. The peak shear stress mobilized from the front face toward the back end for $\sigma_{n0} = 80$ kPa, whereas this mobilization was less significant for $\sigma_{n0} = 50$ kPa, which might be affected by the fitting method. Nevertheless, the location of the peak shear stress for $\sigma_{n0} = 50$ kPa was closer to the back end than for the case of $\sigma_{n0} = 80$ kPa. Moreover, the peak shear stress had higher values for $\sigma_{n0} = 80$ kPa at a given pullout displacement than for $\sigma_{n0} = 50$ kPa, whereas lower shear stress was identified for $\sigma_{n0} = 80$ kPa at the locations near the back end ($S_i > 500$ mm). These observations can be explained as follows. Under higher initial normal stress, the transmission of the elongation of the geogrid is slower due to higher soil resistance. However, in the elongated section, the deformation of the geogrid is more pronounced, which also leads to a higher shear stress. By contrast, because of less resistance provided by the soil particles under lower initial normal stress, the elongation transmits faster toward the back end, with lower peak shear stress but wider distribution of shear stress.

Effect of Fixing Condition

Pullout Force and Normal Stress

The effect of the fixing condition of the back end on the pullout behavior of the geogrid is compared in Fig. 11 by plotting the variations of pullout force versus the pullout displacement in Tests 6, 8, 3, and 9 (Table 2); N50-free denotes an initial normal stress of 50 kPa and that the fixing condition of the back end is free. Before the pullout displacement S_i reached about 5 mm, the variation curves remained close to each other regardless of the fixing condition. Nevertheless, at a given initial normal stress, the pullout force with a fixed back end was higher than with a free back end when $S_i > 5$ mm due to the additional force provided by the fixed clamp at the back end. Furthermore, the pullout behavior of the geogrid with a fixed back end was not influenced by the initial normal stress significantly, as shown by the two close curves with hollow symbols in Fig. 11.

Fig. 12 presents the variations of normal stress with the pullout displacement for the two cases with different fixing conditions of the back end. In spite of the higher pullout force for the case with the fixed back end, its increment of the normal stress was lower than that of the free-back-end case. This indicates that in the test with the free back end, more-significant soil dilatancy was developed because of the more intense movement of soil particles induced by the slippage of the entire geogrid.

Tensile Force and Shear Stress

The measured results of the FBG sensors are depicted in Fig. 13 by the variation of tensile force of geogrid and shear stress at the soil–geogrid interface in Tests 3 and 9 (Table 2). Figs. 13(a and b) show

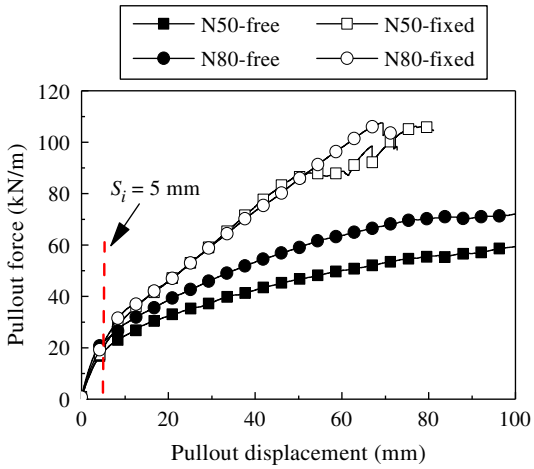

Fig. 11. Comparison of fixing conditions: variations of pullout force with pullout displacement.

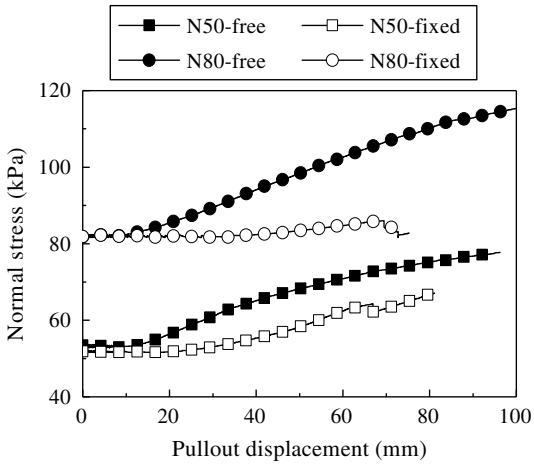

Fig. 12. Comparison of fixing conditions: variations of normal stress with pullout displacement.

the variation of pullout force with pullout displacement at different locations on the geogrid. Unlike the free-back-end case, the area at $S_i > 500$ mm in the fixed condition started to elongate after the pullout displacement increased to 3 mm because of the additional force of the fixed back end. The tensile force distribution along the geogrid length at different pullout displacements [Fig. 13(d)] shows that in the fixed condition, the maximum tensile force developed in the geogrid section closest to the front face at each pullout displacement. In addition, the distribution of the tensile force was more proportional or linear along the geogrid when $S_i > 80$ mm in this condition.

Figs. 13(e and f) compare the distributions of the shear stress along the soil–geogrid interface for the two cases. Quadratic polynomial fitting methods were also applied to fit these data; the coefficients of determination for these curves are presented in Table 3. Totally different distribution modes of shear stress along the geogrid can be identified. In the free-end condition, the peak shear stress mobilized from the front face to the back end as the pullout displacement increased, as illustrated previously. By contrast, in the fixed-end condition at a given pullout displacement, the maximum shear stress was generated in the area closest to the front face, showing a nonlinear decreasing trend of shear stress along the

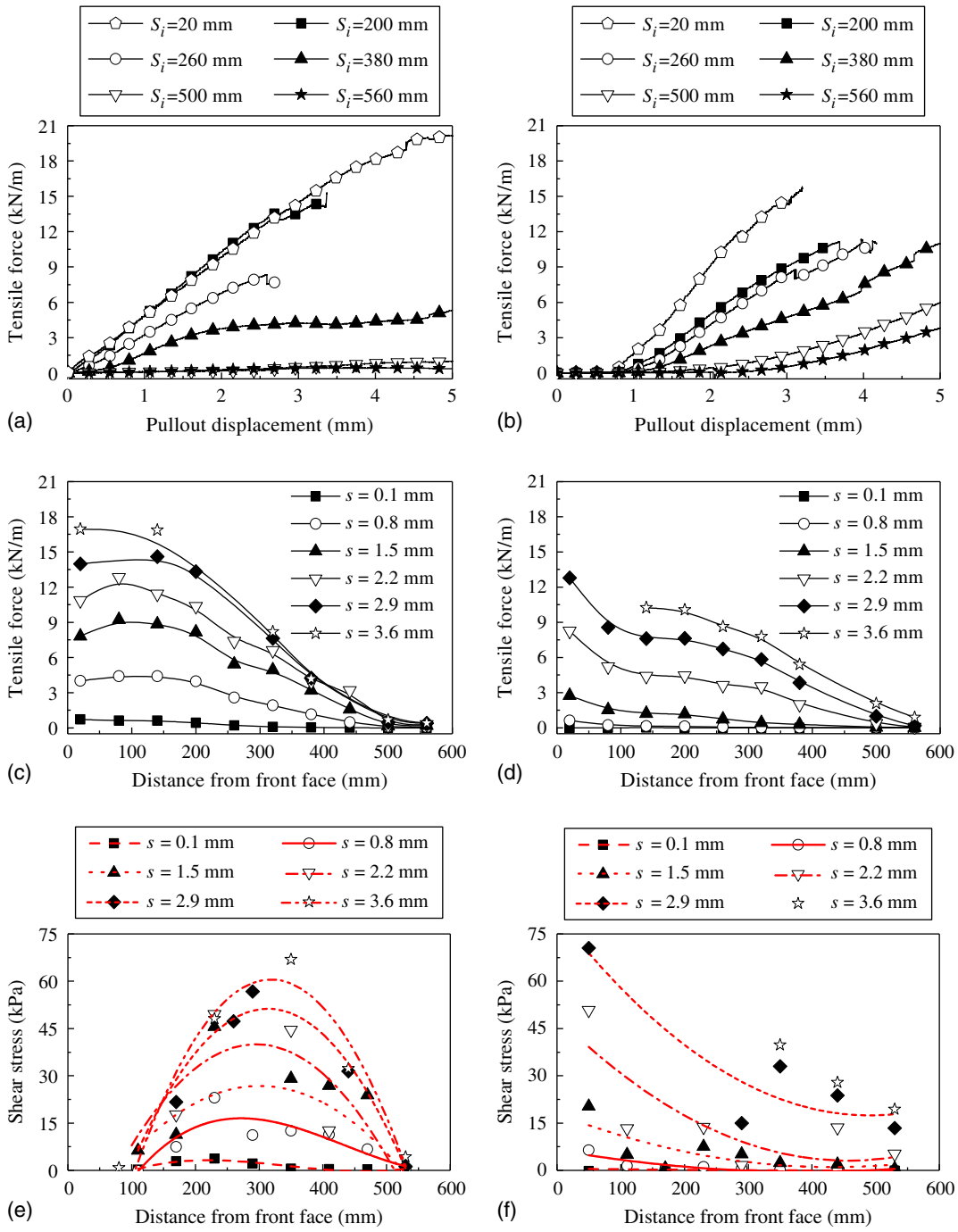

Fig. 13. Comparison of fixing conditions: (a and b) variations of tensile force with pullout displacement; (c and d) variations of tensile force with distance from front face; and (e and f) variations of shear stress with distance from front face. (a, c, and e) indicate the Test 3 with free back end; and (b, d, and f) indicate the Test 9 with fixed back end.

geogrid length toward the back end, which corresponds well with the DEM investigations by Wang et al. (2014). As the pullout displacement increased, the maximum shear stress increased accordingly. In addition, due to the fixed back end, the peak shear stress still developed in the vicinity closest to the front face.

Conclusions

This paper presents an experimental study of soil–geogrid interaction behavior with the application of fiber Bragg grating (FBG) sensors under pullout conditions. Three influencing factors were considered: dry density of soil, initial normal stress, and fixing condition of the back end. During the pullout process, the normal stress was applied using a displacement-controlled mode and the horizontal pullout load was conducted at a constant rate. In the tests, pullout force, pullout displacement, normal stress and wavelength shift of the FBG sensors were directly monitored. The obtained results allow the effects of the aforementioned three influencing factors on the soil–geogrid interaction behaviors to be analyzed.

At a given pullout displacement, the pullout force and the increment of normal stress had higher values for samples with higher dry density, showing more significant dilatancy of the soil. For the

sample with a free back end, the peak shear stress mobilized from the front face toward the back end as the pullout displacement increased. Because of less soil resistance, this mobilization behavior transmitted faster in the looser sample, whereas this sample's peak shear stress values were lower than those of the denser sample.

As the initial normal stress increased, the pullout force increased accordingly. In cases with lower initial normal stress, the mobilization of the peak shear stress transmitted faster, leading to larger values of shear stress near the back end and wider distribution of the shear stress along the geogrid. However, the peak shear stress for the higher initial normal stress remained higher than that for the lower initial normal stress at a given pullout displacement, due to the more significant deformation in the elongated area of the geogrid.

When the back end was fixed, the pullout force was not significantly affected by the initial normal stress, which also had higher values than that of the free-back-end case for a given initial normal stress, due to the additional force provided by the fixed end. Two different modes of shear stress distribution along the soil–geogrid interface were identified in the cases with different fixing conditions of the back end: for the free-end condition, the peak shear stress developed in the middle of the geogrid and transmitted toward the back end as the pullout displacement increased; for the fixed-end condition, the peak shear stress developed at the front face, with a nonlinear decreasing trend along the geogrid toward the back end.

Acknowledgments

This work was carried out with the support of the National Key Research and Development Program of China (2016YFC0800207), the National Natural Science Foundation of China (41472244, 51608188), and the Provincial Key Research and Development Program of Hunan (0105679005).

Notation

The following symbols are used in this paper:

C_c = coefficient of curvature;
C_u = coefficient of uniformity;
F = tensile force across width of geogrid;
F_p = pullout force;
J = stiffness at strain of 2% for geogrid;
S_i = distance from front face of pullout box;
s = pullout displacement;
T_r = tensile force per unit width of geogrid;
T_{ri} = tensile force at back end of ith segment;
T_{ri-1} = tensile force at front end of ith segment;
T_u = ultimate longitudinal tensile strength;
W = width of geogrid;
Δs = distance between FBG sensors;
ε = axial strain of geogrid;
ρ_d = dry density of soil;
σ_{n0} = initial normal stress; and
τ_i = mean shear stress at ith segment.

References

Abdesssemed, M., S. Kenai, and A. Bali. 2015. "Experimental and numerical analysis of the behavior of an airport pavement reinforced by geogrids." *Constr. Build. Mater.* 94: 547–554. https://doi.org/10.1016/j.conbuildmat.2015.07.037.

Abu-Farsakh, M., G. Souci, G. Z. Voyiadjis, and Q. Chen. 2012. "Evaluation of factors affecting the performance of geogrid-reinforced granular base material using repeated load triaxial tests." *J. Mater. Civ. Eng.* 24 (1): 72–83. https://doi.org/10.1061/(ASCE)MT.1943-5533.0000349.

Al-Qadi, I. L., S. H. Dessouky, J. Kwon, and E. Tutumluer. 2012. "Geogrid-reinforced low-volume flexible pavements: Pavement response and geogrid optimal location." *J. Transp. Eng.* 138 (9): 1083–1090. https://doi.org/10.1061/(ASCE)TE.1943-5436.0000409.

Arulrajah, A., M. A. Rahman, J. Piratheepan, M. W. Bo, and M. A. Imteaz. 2014. "Evaluation of interface shear strength properties of geogrid-reinforced construction and demolition materials using a modified large-scale direct shear testing apparatus." *J. Mater. Civ. Eng.* 26 (5): 974–982. https://doi.org/10.1061/(ASCE)MT.1943-5533.0000897.

ASTM. 2015. *Standard test method for determining tensile properties of geogrids by the single or multi-rib tensile method*. ASTM D6637/D6637M. West Conshohocken, PA: ASTM.

ASTM. 2017. *Standard practice for classification of soils for engineering purposes (unified soil classification system)*. ASTM D2487. West Conshohocken, PA: ASTM.

Chen, C., G. R. McDowell, and N. H. Thom. 2014a. "Investigating geogrid-reinforced ballast: Experimental pull-out tests and discrete element modelling." *Soils Found.* 54 (1): 1–11. https://doi.org/10.1016/j.sandf.2013.12.001.

Chen, Q., M. Abu-Farsakh, G. Z. Voyiadjis, and G. Souci. 2013. "Shakedown analysis of geogrid-reinforced granular base material." *J. Mater. Civ. Eng.* 25 (3): 337–346. https://doi.org/10.1061/(ASCE)MT.1943-5533.0000601.

Chen, R. P., J. M. Chen, and H. L. Wang. 2014b. "Recent research on the track-subgrade of high-speed railways." *J. Zhejiang Univ.-Sci. A* 15 (12): 1034–1038. https://doi.org/10.1631/jzus.A1400342.

Chen, R. P., Y. W. Wang, X. W. Ye, X. C. Bian, and X. P. Dong. 2016. "Tensile force of geogrids embedded in pile-supported reinforced embankment: A full-scale experimental study." *Geotext. Geomembr.* 44 (2): 157–169. https://doi.org/10.1016/j.geotexmem.2015.08.001.

Devore, J. L. 2011. *Probability and statistics for engineering and the sciences*, 508–510. 8th ed. Boston: Cengage Learning.

Ferellec, J.-F., and G. R. McDowell. 2012. "Modelling of ballast-geogrid interaction using the discrete-element method." *Geosynth. Int.* 19 (6): 470–479. https://doi.org/10.1680/gein.12.00031.

Ferreira, J. A. Z., and J. G. Zornberg. 2015. "A transparent pullout testing device for 3D evaluation of soil-geogrid interaction." *Geotech. Test. J.* 38 (5): 686–707.

Han, J., A. Bhandari, and F. Wang. 2012. "DEM analysis of stresses and deformations of geogrid-reinforced embankments over piles." *Int. J. Geomech.* 12 (4): 340–350. https://doi.org/10.1061/(ASCE)GM.1943-5622.0000050.

Ho, Y. T., A. B. Huang, and J. T. Lee. 2006. "Development of a fibre Bragg grating sensored ground movement monitoring system." *Meas. Sci. Technol.* 17 (7): 1733–1740. https://doi.org/10.1088/0957-0233/17/7/011.

Hong, C. Y., J. H. Yin, W. Jin, C. Wang, W. H. Zhou, and H. H. Zhu. 2016. "Comparative study on the elongation measurement of a soil nail using optical lower coherence interferometry method and FBG method." *Adv. Struct. Eng.* 13 (2): 309–319. https://doi.org/10.1260/1369-4332.13.2.309.

Huang, B., and R. J. Bathurst. 2009. "Evaluation of soil-geogrid pullout models using a statistical approach." *Geotech. Test. J.* 32 (6): 489–504. https://doi.org/10.1520/GTJ102460.

Hussaini, S. K. K., B. Indraratna, and J. S. Vinod. 2015. "Application of optical-fiber Bragg grating sensors in monitoring the rail track deformations." *Geotech. Test. J.* 38 (4): 20140123. https://doi.org/10.1520/GTJ20140123.

Indraratna, B., L. S. Wijewardena, and A. S. Balasubramaniam. 1993. "Large-scale triaxial testing of greywacke rockfill." *Geotechnique* 43 (1): 37–51. https://doi.org/10.1680/geot.1993.43.1.37.

Kang, X., D. Cambio, and L. Ge. 2012. "Effect of parallel gradations on crushed-rock concrete interface behaviors." *J. Test. Eval.* 40 (1): 119–126. https://doi.org/10.1520/JTE103773.

Lee, W., W. J. Lee, S. B. Lee, and R. Salgado. 2004. "Measurement of pile load transfer using the fiber Bragg grating sensor system." *Can. Geotech. J.* 41 (6): 1222–1232. https://doi.org/10.1139/t04-059.

Leshchinsky, D., B. Imamoglu, and C. L. Meehan. 2010. "Exhumed geogrid-reinforced retaining wall." *J. Geotech. Geoenviron. Eng.* 136 (10): 1311–1323. https://doi.org/10.1061/(ASCE)GT.1943-5606.0000354.

Liu, C. N., J. G. Zornberg, T. C. Chen, Y. H. Ho, and B. H. Lin. 2009. "Behavior of geogrid-sand interface in direct shear mode." *J. Geotech. Geoenviron. Eng.* 135 (12): 1863–1871. https://doi.org/10.1061/(ASCE)GT.1943-5606.0000150.

Lopes, M. L., and M. Ladeira. 1996. "Influence of the confinement, soil density and displacement rate on soil-geogrid interaction." *Geotext. Geomembr.* 14 (10): 543–554. https://doi.org/10.1016/S0266-1144(97)83184-6.

Mamidi, V. R., S. Kamineni, L. N. S. P. Ravinuthala, S. S. Madhuvarasu, V. R. Thumu, V. R. Pachava, and K. Putha. 2014. "Fiber Bragg grating-based high temperature sensor and its low cost interrogation system with enhanced resolution." *Opt. Appl.* 44 (2): 299–308. https://doi.org/10.5277/oa140210.

McDowell, G. R., O. Harireche, H. Konietzky, S. F. Brown, and N. H. Thom. 2006. "Discrete element modelling of geogrid-reinforced aggregates." *Proc. ICE Geotech. Eng.* 159 (1): 35–48. https://doi.org/10.1680/geng.2006.159.1.35.

Mihailov, S. J. 2012. "Fiber Bragg grating sensors for harsh environments." *Sensors* 12 (2): 1898–1918. https://doi.org/10.3390/s120201898.

Moraci, N., and P. Recalcati. 2006. "Factors affecting the pullout behaviour of extruded geogrids embedded in a compacted granular soil." *Geotext. Geomembr.* 24 (4): 220–242. https://doi.org/10.1016/j.geotexmem.2006.03.001.

Nichols, J. M., S. T. Trickey, M. Seaver, and L. Moniz. 2007. "Use of fiber-optic strain sensors and holder exponents for detecting and localizing damage in an experimental plate structure." *J. Intel. Mat. Syst. Struct.* 18 (1): 51–67. https://doi.org/10.1177/1045389X06064354.

Palmeira, E. M. 2009. "Soil-geosynthetic interaction: Modelling and analysis." *Geotext. Geomembr.* 27 (5): 368–390. https://doi.org/10.1016/j.geotexmem.2009.03.003.

Qian, Y., J. Han, S. K. Pokharel, and R. L. Parsons. 2013. "Performance of triangular aperture geogrid-reinforced base courses over weak subgrade under cyclic loading." *J. Mater. Civ. Eng.* 25 (8): 1013–1021. https://doi.org/10.1061/(ASCE)MT.1943-5533.0000577.

Sugimoto, M., and A. M. N. Alagiyawanna. 2003. "Pullout behavior of geogrid by test and numerical analysis." *J. Geotech. Geoenviron. Eng.* 129 (4): 361–371. https://doi.org/10.1061/(ASCE)1090-0241(2003)129:4(361).

Sugimoto, M., A. M. N. Alagiyawanna, and K. Kadoguchi. 2001. "Influence of rigid and flexible face on geogrid pullout tests." *Geotext. Geomembr.* 19 (5): 257–277. https://doi.org/10.1016/S0266-1144(01)00011-5.

Sun, X., J. Han, and R. Corey. 2017a. "Equivalent modulus of geogrid-stabilized granular base back-calculated using permanent deformation." *J. Geotech. Geoenviron. Eng.* 143 (9): 06017012. https://doi.org/10.1061/(ASCE)GT.1943-5606.0001761.

Sun, Y., H. Xu, P. Gu, and W. Hu. 2017b. "Application of FBG sensing technology in stability analysis of geogrid-reinforced slope." *Sensors* 17 (3): 597. https://doi.org/10.3390/s17030597.

Teixeira, S. H. C., B. S. Bueno, and J. G. Zornberg. 2007. "Pullout resistance of individual longitudinal and transverse geogrid ribs." *J. Geotech. Geoenviron. Eng.* 133 (1): 37–50. https://doi.org/10.1061/(ASCE)1090-0241(2007)133:1(37).

Trinh, V. N., A. M. Tang, Y. J. Cui, J. C. Dupla, J. Canou, N. Calon, L. Lambert, A. Robinet, and O. Schoen. 2012. "Mechanical characterisation of the fouled ballast in ancient railway track substructure by large-scale triaxial tests." *Soils Found.* 52 (3): 511–523. https://doi.org/10.1016/j.sandf.2012.05.009.

Wang, H. L., R. P. Chen, W. Cheng, S. Qi, and Y. J. Cui. 2018a. "Full-scale model study on variations of soil stress in geosynthetic-reinforced pile-supported track-bed with water level change and loading cycles." *Can. Geotech. J.*, in press. https://doi.org/10.1139/cgj-2017-0689.

Wang, H. L., R. P. Chen, S. Qi, W. Cheng, and Y. J. Cui. 2018b. "Long-term performance of pile-supported ballastless track-bed at various water levels." *J. Geotech. Geoenviron. Eng.* 144 (6): 04018035. https://doi.org/10.1061/(ASCE)GT.1943-5606.0001890.

Wang, H. L., Y. J. Cui, F. Lamas-Lopez, J. C. Dupla, J. Canou, N. Calon, G. Saussine, P. Aimedieu, and R. P. Chen. 2017. "Effects of inclusion contents on resilient modulus and damping ratio of unsaturated track-bed materials." *Can. Geotech. J.* 54 (12): 1672–1681. https://doi.org/10.1139/cgj-2016-0673.

Wang, H. L., Y. J. Cui, F. Lamas-Lopez, J. C. Dupla, J. Canou, N. Calon, G. Saussine, P. Aimedieu, and R. P. Chen. 2018c. "Investigation on the mechanical behavior of track-bed materials at various contents of coarse grains." *Constr. Build. Mater.* 164: 228–237. https://doi.org/10.1016/j.conbuildmat.2017.12.209.

Wang, H. L., Y. J. Cui, F. Lamas-Lopez, J. C. Dupla, J. Canou, N. Calon, G. Saussine, P. Aimedieu, and R. P. Chen. 2018d. "Permanent deformation of track-bed materials at various inclusion contents under large number of loading cycles." *J. Geotech. Geoenviron. Eng.* 144 (8): 04018044. https://doi.org/10.1061/(ASCE)GT.1943-5606.0001911.

Wang, Z., F. Jacobs, and M. Ziegler. 2014. "Visualization of load transfer behaviour between geogrid and sand using PFC^{2D}." *Geotext. Geomembr.* 42 (2): 83–90. https://doi.org/10.1016/j.geotexmem.2014.01.001.

Wang, Z.-F., J. Wang, Q.-M. Sui, X.-M. Liang, L. Jia, S.-C. Li, and S.-D. Lu. 2015. "Development and application of smart geogrid embedded with fiber Bragg grating sensors." *J. Sensors* 2015: 108209. https://doi.org/10.1155/2015/108209.

Wilson-Fahmy, R. F., R. M. Koerner, and W. A. Harpur. 1995. "Long-term pullout behavior of polymeric geogrids." *J. Geotech. Eng.* 121 (10): 723–728. https://doi.org/10.1061/(ASCE)0733-9410(1995)121:10(723).

Wilson-Fahmy, R. F., R. M. Koerner, and L. J. Sansone. 1994. "Experimental behavior of polymeric geogrids in pullout." *J. Geotech. Eng.* 120 (4): 661–677. https://doi.org/10.1061/(ASCE)0733-9410(1994)120:4(661).

Zhang, J., and N. Yasufuku. 2009. "Evaluation of rainfall infiltration and compaction effect on soil-geogrid interaction behavior." *Geosynth. Eng. J.* 24: 61–68. https://doi.org/10.5030/jcigsjournal.24.61.

Zhang, J., N. Yasufuku, and H. Ochiai. 2007. "A few considerations of pullout test characteristics of geogrid reinforced sand using DEM analysis." *Geosynth. Eng. J.* 22: 103–110. https://doi.org/10.5030/jcigsjournal.22.103.

Zhao, L.-S., W.-H. Zhou, B. Fatahi, X.-B. Li, and K.-V. Yuen. 2016. "A dual beam model for geosynthetic-reinforced granular fill on an elastic foundation." *Appl. Math. Model.* 40 (21–22): 9254–9268. https://doi.org/10.1016/j.apm.2016.06.003.